PCCP

ROYAL SOCIETY OF CHEMISTRY

PAPER

View Article Online
View Journal | View Issue

Cite this: *Phys. Chem. Chem. Phys.*, 2026, **28**, 101

Toward a mechanistic understanding of bioluminescence: a theoretical study of furimazine oxidation and luminescence

Alessandro Bonardi, *[a,b] Michele Turelli,[a] Anna Ranaudo, [c] Giorgio Moro,[c] Claudio Greco, [c] Ilaria Ciofini, *[a] Ugo Cosentino*[c] and Carlo Adamo [a]

Received 6th October 2025,
Accepted 17th November 2025

DOI: 10.1039/d5cp03858h

rsc.li/pccp

The desirable attributes of luciferin–luciferase systems for bioluminescence imaging include their high luminescence intensities, minimal background signals, and compact enzyme sizes, with robust structural stability under experimental conditions. The NanoLuc–furimazine system has emerged as a promising candidate, fulfilling all these requirements. However, the detailed reaction mechanism leading to furimazine oxidation and the nature of the luminescent species remain largely unknown. Current understanding is limited to the formation of an excited-state product as a consequence of furimazine oxidation. In this context, this study exploits density functional theory and its time-dependent formalism to identify reactive species and analyze the possible mechanisms associated with this process in a solution, including the investigation of two possible oxygenation pathways and the formation of subsequent excited-state furimamide. For completeness, three different protonation states of furimamide were considered, and its zwitterionic form emerged as a promising candidate for emission applications, offering new insights and establishing a foundation for the future extension of this study in a protein environment.

1. Introduction

Bioluminescence is a natural phenomenon that has captivated researchers because of its multiple applications.[1–4] It consists of light emission by living organisms, and it not only serves various ecological roles, such as predator deterrence, mate attraction, and symbiotic relationships, but has also been deployed for numerous applications in biotechnology.[1,5] Despite their chemical diversity, bioluminescent systems share a common feature: the ability to convert chemical energy into photons. At the heart of bioluminescence lies the luciferase-catalyzed oxidation of a substrate known as luciferin, resulting in the production of a high-energy intermediate, emitting light in the visible range.[6] Luciferases are found across a wide range of organisms, from marine animals and terrestrial insects to fungi and bacteria, each exhibiting distinct biochemical properties and reaction mechanisms even when working on the same substrate.[7–11] Understanding the intricate reaction mechanisms of luciferases is pivotal for both fundamental biological research and practical applications. This is because a better mechanistic knowledge can guide the design of recombinant luciferases with enhanced properties, such as increased stability, altered emission spectra, and improved substrate affinity, further broadening their applicability in research and the industry.[12–15] Up to now, many artificial luciferases have been obtained with a directed evolution approach since the lack of detailed knowledge of the underlying reaction mechanism has prevented the rational design of the enzyme to improve their performances.[16,17]

A well-known and successful example of this approach is the NanoLuc–furimazine pair, a synthetic luciferase–luciferin system that has been obtained from OLuc-Coelenterazine, the natural system responsible for *Oplophorus gracilirostris'* bioluminescence.[18] NanoLuc is very popular in bioluminescent assays, enabling the highly sensitive detection of various biological processes, from gene expression and protein interactions to cell viability and signalling pathways.[3,19–21] The remarkable sensitivity and specificity of luciferase-based assays stem from the inherent properties of bioluminescent reactions, which produce low background noise and can be easily quantified using luminescence detectors. Additionally, the NanoLuc–furimazine pair shows significantly improved traits with regard to the most desirable properties for bioluminescent assays' key compounds. Indeed, compared with the firefly luciferase, the most studied enzyme of this class, not only is NanoLuc stable at a wider range of temperatures and pH, it is also smaller (16 kDa *vs.* 62 kDa) and, on top of that,

---

[a] *Chimie ParisTech – PSL, PSL University, CNRS, Institute of Chemistry for Health and Life Sciences, F-75005 Paris, France. E-mail: ilaria.ciofini@chimieparistech.psl.eu*

[b] *Department of Material Sciences, Milano-Bicocca University, I-20126 Milano, Italy. E-mail: a.bonardi3@campus.unimib.it*

[c] *Department of Earth and Environmental Sciences, Milano-Bicocca University, I-20126 Milano, Italy. E-mail: ugo.cosentino@unimib.it*

100 times brighter.[3,18] These properties are the result of various steps of directed evolution performed on the enzyme structure, but also of modifications on the substrate, furimazine (schematically represented in Scheme 1), which is a synthetic coelenterazine analogue that efficiently undergoes oxidation to produce light.

Despite the advantages of this system, the detailed reaction mechanism leading to the oxidation of furimazine, resulting in photon emission, remains poorly understood.[22,23] The current experimentally confirmed knowledge is limited to the general concept that molecular oxygen reacts with furimazine, forming an excited-state intermediate that decays to emit light.[23]

To date, a reaction mechanism has been proposed for other luciferases containing the same core,[4,8] that is, imidazopyrazinone (Scheme 1, black), but no detailed study has specifically addressed the reaction mechanism at work for furimazine, which could be determined using the different substituents.

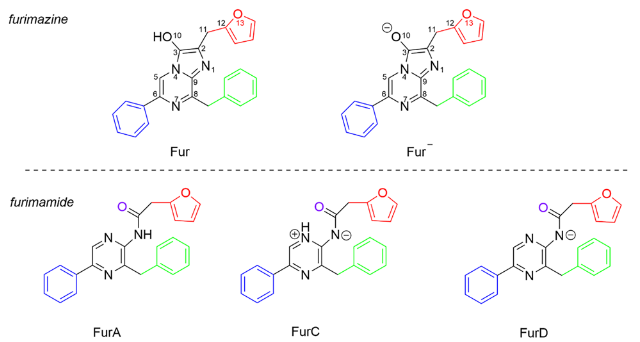

Scheme 1 Schematic of furimazine (in its more stable enol form, Fur[22]) and its corresponding deprotonated form, **Fur**$^-$, including the labelling scheme together with the postulated product (furimamide) in its neutral (**FurA**), zwitterionic (**FurC**) and anionic (**FurD**) forms. In all systems, the imidazopyrazinone core is depicted in black.

As reported in Scheme 2, the mechanism proposed for the oxidation of the imidazopyrazinone substrates consists of a complex multi-step reaction, which can be broken down into three key steps: (i) deprotonation, (ii) oxygenation and formation of a dioxetanone intermediate and (iii) decomposition and light emission.

In detail, first, the imidazopyrazinone core is expected to undergo a deprotonation catalysed by the enzyme, which is necessary to activate the substrate,[4,24,25] followed by an oxygenation, leading to the formation of a peroxy intermediate. Previous studies on luciferin suggest that this step involves a single electron transfer (SET) from the anionic luciferin to an oxygen molecule, leading to the formation of a superoxide anion that reacts with the imidazopyrazinone core to form the corresponding peroxide.[26,27] In coelenterazine-derived systems, oxygen is expected to attack preferentially the C_2 position, and the resulting peroxy intermediate undergoes an intramolecular cyclization reaction, forming a highly strained dioxetanone ring.[8] This high-energy intermediate (HEI) is key to the bioluminescent reaction. Indeed, the instability of the dioxetane ring is such that it readily decomposes, leading to the formation of an excited-state product. Computational studies, including density functional theory (DFT) calculations, performed on these imidazopyrazinone substrates have shown that the formation and subsequent breakdown of the dioxetane ring is indeed energetically favourable and is the primary source of the energy required for photon emission.[28,29] The exact pathway of decomposition can vary slightly depending on the specific luciferase, but the general principle remains the same. The excited oxyluciferin molecule relaxes back to its ground state, emitting a photon in the process. The wavelength of the emitted light is determined

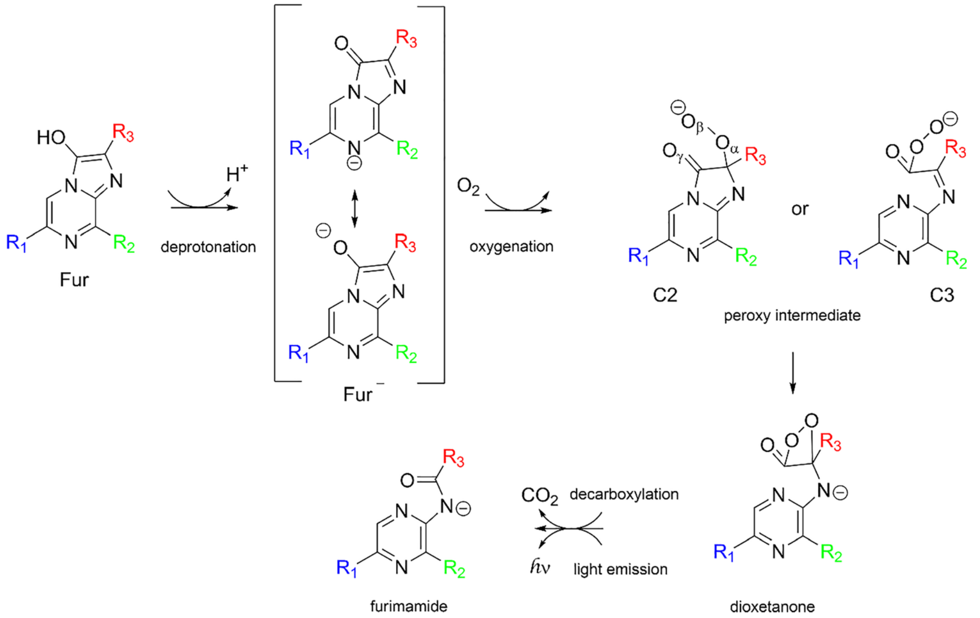

Scheme 2 Schematic of the furimazine oxidation and the decomposition mechanism responsible for the observed luminescence. In all systems, the imidazopyrazinone core is depicted in black. R_1, R_2 and R_3 are depicted in Scheme 1.

by the specific structure of the luciferin and the environment within the luciferase active site.

Starting from the literature data collected on related systems, our aim in the present work is to disclose the mechanism at work in the case of furimazine and understand the origin of its blue luminescence experimentally characterized by an emission peak at around 460 nm.[18]

To this end, we resorted to the density functional theory (DFT) and time-dependent DFT (TD-DFT) approaches to accurately and efficiently model the electronic and structural changes occurring during the ground and excited state reactions responsible for bioluminescence.

We specifically focused on getting a detailed picture of the furimazine reactivity in a DMSO solution, since this solvent is commonly used in the experimental studies of chemiluminescence.[1,24,30,31] Starting from the anionic form of furimazine (Scheme 2), two possible binding sites (C_2 and C_3) were considered for the initial oxygen species attack and the subsequent formation of the dioxetanone ring. Next, three different dioxetanone decomposition channels, leading to three different forms of furimamide, were explored in order to disclose the nature of the emitting species. Indeed, owing to the lack of experimental data, the protonation state of the emissive product is not yet fully disclosed. Previous theoretical studies of the possible protonation states of the furimamide product point out that the neutral (**FurA**, Scheme 1) and the zwitterionic (**FurC**, Scheme 1) forms are expected to be the dominant ones in the entire pH range in the aqueous solution in the ground state (GS) and excited state (ES), respectively.[32] This is the reason these two forms were first considered as the products of the dioxetanone decomposition. In addition to them, the corresponding amide anion (**FurD**, Scheme 1) was also considered as a possible emissive product, in analogy to what was proposed for other luciferin–luciferase systems.[33,34] Furthermore, since the reaction mechanism starts from deprotonated furimazine, it is not aberrant to postulate the presence of such an anionic species as a product. Our previous work on the emission properties of furimamide in a protein environment suggests that both the zwitterionic form (**FurC**) and the anionic form (**FurD**) have emission spectral features close to the experimental one, while the neutral species (**FurA**) could not be present in the protein environment.[22]

Overall, our results indicate that energetically plausible reaction paths can be found, leading to the formation of all the products identified. The nature of the most relevant intermediates and TS has been identified, and possible ways of stabilizing relevant species (thanks to H bonds or electrostatic interactions with the enzymes) are provided.

Such insights are crucial for enhancing our understanding of the fundamental processes underpinning bioluminescence and could pave the way for engineering-improved bioluminescent systems with tailored properties for specific applications.

2. Computational details

DFT and TD-DFT calculations were used to characterize ground state (GS) and excited state (ES) potential energy surfaces, respectively. All calculations were performed with the Gaussian16 package.[35] The range-separated hybrid functional CAM-B3LYP[36] and the 6-31+G(d,p)[37–40] basis set were used for all DFT and TD-DFT calculations. This functional (CAM-B3LYP) has been selected since it has already been used on similar systems (including furimazine derivatives),[25,32,41,42] providing accurate optical properties. Furthermore, range-separated hybrids provide more accurate barrier heights than most of the so-called hybrid functionals and are expected to give a better description of the PES far from the Franck–Condon region.[43]

Solvent effects were taken into account by means of the polarizable continuum model (PCM)[44] using the Conductor Like model (CPCM).[45,46]

The unrestricted Kohn–Sham (UKS) formalism was used to treat open shell systems, and the broken symmetry (BS) technique was applied to describe open shell singlets.

Structural optimization and subsequent harmonic frequency calculations, as well as zero-point vibrational energy (ZPE) and thermodynamic properties, were computed at this level of theory at the GS and ES. Transition states were located on the GS closed–shell singlet PES using the QST3 (Quadratic Synchronous Transit 3) method. The nature of the transition states (TS) obtained was confirmed by Intrinsic Reaction Coordinate (IRC) calculations, to verify that each transition state was effectively connecting the corresponding minima on the GS or ES potential energy profiles. To study the chemiluminescence process occurring with the decomposition of the dioxetanone intermediate, as the latter is supposed to afford the final product in the excited state, the final-product structure was determined on the ES (S_1) PES, and the TS was found by means of QST3 between this ES product and the corresponding GS dioxetanone. The energy gaps between the GS PES and the ES PES along the dioxetanone decomposition pathways have been evaluated with TD-DFT single points, performed on the geometries obtained from the IRC calculations.

3. Results and discussion

3.1 Furimazine oxidation and formation of the dioxetanone intermediate

As previously reported,[4,24,25] the first step of the entire reaction is the deprotonation of **Fur** (Scheme 1). In a previous study,[22] we demonstrated that the enol form of furimazine is more stable than the keto form, since it is stabilized in the protein environment by a H bond with the sidechain of an aspartate residue that may also catalyse the deprotonation. We, therefore, assumed that the starting reagent is the deprotonated enolic form of furimazine, hereafter labelled as **Fur**$^-$.

Previous studies on luciferins and other imidazopyrazinone-containing systems[26,27] have advocated the activation of the oxygen molecule through a SET from the so-formed **Fur**$^-$, leading to the formation of a superoxide radical (O_2^-) and a furimazine radical (**Fur**$^\bullet$). For this reason, different electronic states have been computed for the initial steps of the reaction. They include (i) a closed–shell singlet state; (ii) an open–shell singlet state, corresponding to a SET from the **Fur**$^-$ to the O_2 molecule and the subsequent antiferromagnetic coupling of the radicals, leading to the formation of ^{1}(**Fur**$^{\bullet\uparrow}$-O_2^-); and (iii) a triplet state potentially corresponding to either $^3O_2$ and **Fur**$^-$ or a ferromagnetically coupled system after SET, that is ^{3}(**Fur**$^{\bullet\uparrow}$-O_2^-). Notably, the initial O_2 placement was performed manually near the C_2–C_3 bond, with different starting positions being tested, followed by full geometry optimization. The lowest-energy optimized geometry was kept as the RC structure. As far as it concerns the different spin states, the open–shell singlet state (ii) was obtained *via* broken symmetry calculations, while the triplet state (iii) was obtained simply by imposing a total spin multiplicity of 3.

As previously stated, the SET is followed by the formation of an O–C bond, which can involve either C_2 or C_3, the former being considered the better binding site for O_2 in other systems.[8] The two possibilities have thus been considered.

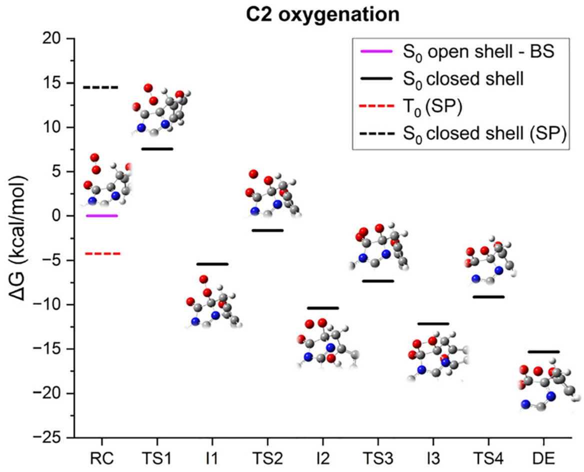

Fig. 1 Free-energy profile computed for the C_2 oxygenation of furimazine (CAM-B3LYP level in DMSO using the 6-31+G(d,p) basis set). Energy of the optimized geometry for the open–shell singlet exciplex used as a reference. The label SP stands for single point energy calculations. Corresponding IRC plots are reported in the SI.

The corresponding computed PES for the subsequent process leading to the formation of the dioxetanone intermediate is depicted in Fig. 1 in the case of an attack in the C_2 position. In order to follow the bond formation, we considered the PES, starting from the reactive optimized open–shell singlet ^{1}(**Fur**$^{\bullet\uparrow}$-O_2^-), labelled BS and reported in purple in Fig. 1, and evaluated, as a single point, the lowest-energy triplet state, labelled T0 and reported in red dashed lines in Fig. 1. The latter corresponds essentially to a $^3O_2$ and **Fur**$^-$. The closed–shell singlet computed as a Single Point is also reported in the same figure as black dashed lines.

The reaction starts with the coordination of the oxygen molecule ($^3O_2$) to the furimazine anion (**Fur**$^-$). Initially, no SET spontaneously occurred from **Fur**$^-$ to the oxygen molecule, as indicated by the fact that the triplet state had the lowest energy. This state thus corresponds to a **Fur**$^-$-$^3O_2$ adduct. The corresponding optimized activated SET complex ^{1}(**Fur**$^{\bullet\uparrow}$-O_2^-) is actually computed at roughly 5 kcal mol^{-1} above the triplet. Nonetheless, as soon as the bond with a carbon atom of furimazine (here in the C_2 position) starts to form, the singlet–triplet energy gap decreases. A decrease in the spin density on the oxygen molecule and an increase in the oxygen–oxygen distance occur just before reaching **TS1** (Fig. 2).

At this point, the triplet and the singlet states also degenerate (Fig. S1). The overall barrier for this activation process is thus 7.6 kcal mol^{-1} from the optimized diradical (18.4 kcal mol^{-1} from the optimized triplet), meaning that it is accessible under standard conditions. Furthermore, in the presence of the protein environment, this barrier could be further lowered, since the first transition state displays a more strongly localized negative charge on the oxygen atom, which could be stabilized by the presence of a positively charged residue or by the formation of an H-bond with the enzyme.

Starting from this transition state (**TS1**), the peroxide intermediate is already formed (as evident from the analysis of the

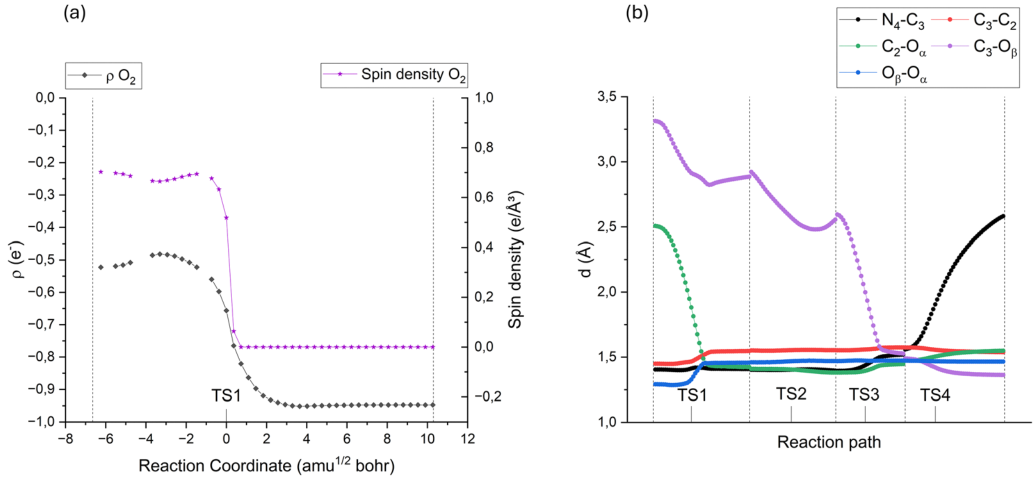

Fig. 2 Evolution along the profile of the furimazine C_2 oxygenation: (a) Mulliken charge and spin density computed on the O_2 fragment for the first step of the reaction along the singlet biradical profile and (b) relevant structural parameters. Refer to Schemes 1 and 2 for the labelling.

global charge on the furimazine fragment, reported in SI), and the system is evolving on the closed–shell ground-state potential energy surface, with the corresponding triplet state lying above by more than 30 kcal mol^{-1} (see SI). Consistently, no spin density is detected on the oxygen atoms nor elsewhere on the molecule.

During the formation of the **I1** intermediate, a shortening of the C_2–O_α distance, accompanied by the elongation of the C_2–C_3 bond and especially the O_α–O_β one, is computed, which is consistent with the formation of a peroxide species.

After the formation of the C_2–O_α bond (**I1**), the reaction proceeds with the bending and rotation of the peroxy fragment, leading the O_β atom towards the imidazopyrazinone core to allow the formation of the C_3–O_β bond. This process occurs in two steps characterized by very small reaction barriers (all below 4 kcal mol^{-1}) corresponding to **TS2** and **TS3**.

Overall, we observe a reduction in the C_3–O_β distance, resulting from the modification of the O_β–O_α–C_2–C_3 dihedral, and a small reduction in the C_2–O_α bond length, as shown in Fig. S2.

From the **I3** intermediate, the O_β–C_3 bond is actually formed, as can be easily seen from the distance trends reported in Fig. S3c, combined with the strong reduction in the dihedral angle, O_β–O_α–C_2–C_3 (Fig. S3d). This step leads to a redistribution of the electron density, as certified by the relevant change in the charge of the oxygen fragment (Fig. S3b), the lengthening in the N_4–C_3 distance and the decrease in the C_6–C_5–N_4–O dihedral. After the formation of the four-membered ring (**I3**), the last step corresponds to the cleavage of the N_4–C_3 bond, leading to the formation of the dioxetanone anion (**DE**), the only intermediate that has been experimentally detected in similar systems.[47] The geometrical parameters showing the most evident changes during this final step are, as expected, the N_4–C_3 and the C_3–O_β distances. A loss of the coplanarity of the O_γ atom with respect to the central core, as well as a redistribution of the negative charge, located exclusively on the oxygen atoms in the peroxy intermediate, on the entire molecule, can also be noted.

Before proceeding further, it is worthwhile to mention that an oxygenation path on the C_3 position cannot be *a priori* excluded for the formation of the same dioxetanone intermediate. The corresponding reaction profile has thus been computed and is reported in Fig. 3, while Mulliken global charge on O_2, together with relevant structural parameters, are reported in Fig. S5 and S6.

The C_2 and C_3 reaction pathways necessarily differ, since C_3 cannot form an additional bond with an oxygen moiety without breaking an existing one. In this case, the formation of the C_3–O_β bond is simultaneously occurring with the elongation not only of the C_2–C_3 and O_α–O_β ones, similarly to the C_2 mechanism, but also of the N_4–C_3 bond, which is progressively broken to give a new intermediate (**I1′**).

The analysis of the computed Mulliken charges and spin density on the oxygen molecule fragment shows that the **I1′** intermediate, formed as a result of the first step of the reaction, corresponds to a peroxide. The presence of another oxygen (O_γ) on the carbon (C_3) bearing the peroxide anion group determines a reduction of the charge localized on O_α and O_β (Fig. S5b), which highlights the charge transfer and back charge transfer process taking place during this step.

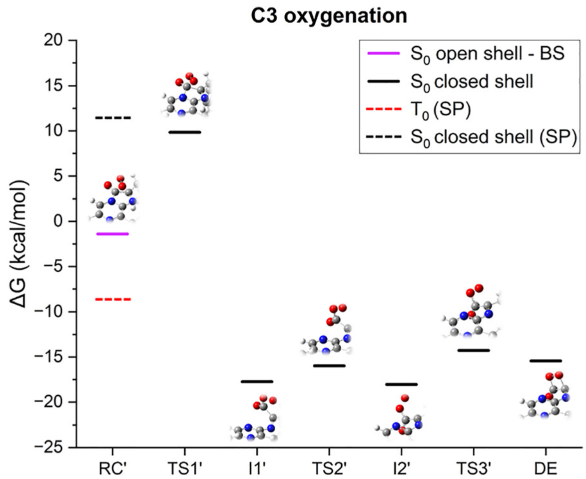

Fig. 3 Free-energy profile computed for the C_3 oxygenation of furimazine (CAM-B3LYP level in DMSO using the 6-31+G(d,p) basis set). For an easier comparison, the same energy reference presented in Fig. 1 is applied. Corresponding IRC plots are reported in the SI.

This intermediate is produced after a practically barrierless rotation of the O_2 moiety to a second intermediate (**I2′**) that easily evolves to the **DE** intermediate with a barrier of only 3.8 kcal mol^{-1}. Indeed, a remarkable detail of this last step is the fact that the C_2–O_α distance is the only structural parameter significantly modified, which is probably the reason behind the low energy barrier associated with it.

Notably, in the case of the C_3, the conversion between the triplet and singlet PES, corresponding first to the formation of the superoxide radical and next to the peroxide intermediate, occurs earlier than in the case of the C_2 attack. In the C_3 pathway, indeed, the **TS1′** is already located on the singlet potential energy curve since the crossing between the triplet and closed–shell singlet curves takes place before the transition state, as confirmed by the results of a scan along the distance C_3–O_β reported in the SI (Fig. S7). According to those results, in fact, the triplet and singlet energy surfaces cross when the C_3–O distance equals 2.10 Å, that is, before **TS1′**, when the distance is 1.62 Å. The closed–shell character of the transition state, then, is further confirmed by the fact that the closer O_2 gets to C_3, the lower the spin density on the O_2 fragment.

Overall, the main difference between the C_2 and the C_3 pathways is in the energy trends: in the case of C_2 oxygenation, the process requires four steps, and almost each step is exergonic, while in the case of C_3, the steps are three, with only the first being strongly exergonic. Furthermore, in the case of the C_2 mechanism, the highest barrier (corresponding to the O_2 attack) is smaller than the corresponding one on the C_3 path (7.6 kcal mol^{-1} with respect to 11.0 kcal mol^{-1}). Despite these differences, both pathways are expected to be feasible under standard conditions and possibly contribute to the formation of the final intermediate, the anionic dioxetanone, which is actually the key HEI, leading to the chemiluminescent process.

3.2 Chemiluminescence from the decomposition of the dioxetanone intermediate

The final step of the reaction leading to chemiluminescence and CO_2 release is the decomposition of the high-energy dioxetanone intermediate. This process has been the subject of high-quality theoretical investigations, mainly performed on simplified models constituted by the dioxetanone core,[48,49] as well as computational investigations on related substrates at a relatively low level of theory.[25,28,41,42] A very simplified and schematic view of the overall process is given in Scheme 3: as the C–C and O–O bonds elongate, the gap between the PES of the GS and ES gets closer to zero, allowing for a crossing between the two around the transition state geometry. In this study, we specifically focus on the analysis of two different aspects: (i) the influence of the substituents (and thus the effect of the inclusion of the full structure of the furimazine skeleton) on this decomposition and (ii) the definition of the nature of the emitting species.

Either the C_2 or C_3 oxygenation pathway leads to the formation of an anionic dioxetanone species (**DE**), but the protein environment could cause its protonation. Thus, it is necessary to account for the different possible protonation states of the dioxetanone intermediate, including the neutral form, labelled **DE$_A$**, and the zwitterionic form, labelled **DE$_C$**. To this end, we have studied all three corresponding decomposition pathways in order to check the viability of the formation of different furimamides (**FurA**, **FurC** and **FurD**, Scheme 1) as emitting species.

Owing to the size of the **DE** intermediates, TD-DFT was considered a sustainable and sufficiently accurate approach to get insights into the decomposition and light emission processes. However, we are clearly aware of the limitations of this method in exactly locating conical intersection points on the PES and describing ESs with diradical character. Nonetheless, we expect this level of theory to be able to (1) locate the region where the GS PES gets close (in the vicinity of the TS) to the ES surface, allowing the generation of excited-state intermediates (as postulated for the dioxetanone core), and (2) describe the excited-state relaxation and the corresponding ES products, thereby allowing to define the nature of the emitting species.

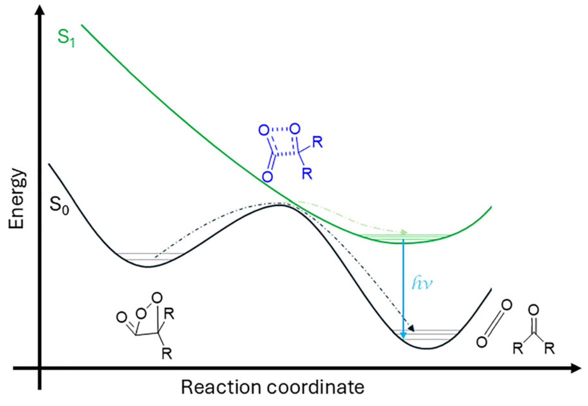

Scheme 3 Simplified picture of the chemiluminescence occurring from a dioxetanone high-energy intermediate.

As indicated in Section 2, we thus resorted to the following procedure: (i) the geometries of the **DE** intermediates were optimized on the GS PES, (ii) the Furimamide + CO_2 exciplex geometries were optimized on the ES PES, and (iii) the Transition State was found with QST3 between the two on its GS PES.

First of all, let us consider the two neutral forms of the **DE** intermediates leading to the formation of the neutral (**FurA**) and zwitterionic (**FurC**) furimamides. The corresponding potential energy profiles are depicted in Fig. 4.

Notably, these starting **DE** intermediates (**DE$_A$** and **DE$_C$**) are not isoenergetic, since the protonation of N_4 (leading to **DE$_C$**) is a less favourable option than the protonation of N_1 (giving **DE$_A$**). In DMSO, the free energy difference between the two structures is computed to be 12.1 kcal mol^{-1} in favour of **DE$_A$**, although the interaction with the enzyme may alter this relative stability.

As evident from Table 1, from a structural point of view, **DE$_A$** and **DE$_C$** are overall very similar. Both species share an identical C_2–C_3 bond length (around 1.54 Å), and the O_α–O_β distance differs by only 0.01 Å (1.47 Å in **DE$_A$** *vs.* 1.46 Å in **DE$_C$**). Furthermore, the torsion values confirm a high degree of coplanarity for the atoms belonging to the four-membered ring and the O_γ in both cases, and no significant structural differences are observed with respect to these parameters. The most pronounced and evident difference lies in the orientation of the dioxetanonic ring with respect to the central core of the molecule, measured by the C_9–N_1–C_2–O_α dihedral. This dihedral is computed to be around 61° in **DE$_A$** compared to only 22° in **DE$_C$**. Indeed, in the case of the **DE$_C$** structure, an intramolecular hydrogen bond between the N_4–H group and O_α is formed.

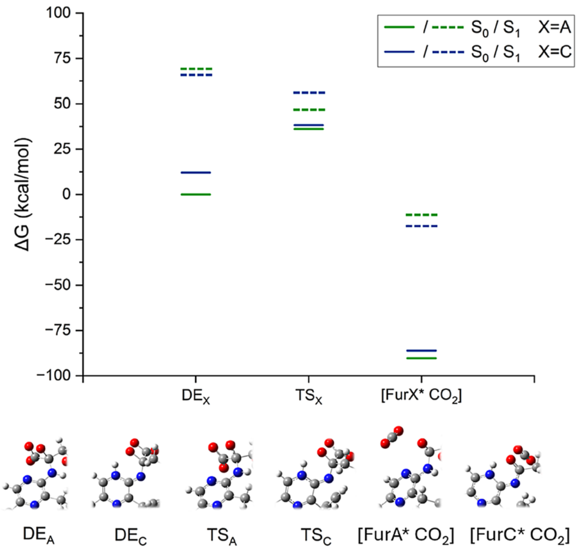

Fig. 4 Free-energy profiles corresponding to the **DE$_A$** and **DE$_C$** decomposition, leading to the formation of **FurA** and **FurC**, respectively. The GS (S_0) free energy of the optimized **DE$_A$** molecule is used as the reference. All calculations are performed at the CAM-B3LYP 6-31+G(d,p) level of theory in DMSO.

The analysis of the GS PES allows us to locate the first TS corresponding to the dissociation of the O_β–O_α bond for both species. In the case of $\mathbf{DE_A}$, this TS ($\mathbf{TS_A}$) lies 36.1 kcal mol^{-1} higher in energy than that of $\mathbf{DE_A}$, while for $\mathbf{DE_C}$, a relatively small barrier is found (26.2 kcal mol^{-1}), mostly due to the lower stability of $\mathbf{DE_C}$ compared with that of $\mathbf{DE_A}$.

These barriers are actually in the same energy range as that computed for the decomposition of another neutral dioxetanone derivative.[50]

As it was for the corresponding **DE**s, also in the case of $\mathbf{TS_A}$ and $\mathbf{TS_C}$, no significant structural differences can be noticed (Table 1). The C_2–C_3 bond length is the same, as its cleavage is after the breaking of the O_α–O_β bond. The latter slightly differs; it is more elongated in $\mathbf{TS_A}$ than in $\mathbf{TS_C}$ (2.10 Å *vs.* 1.94 Å). This feature points out that the O–O elongation process starts earlier in the case of the **FurC** formation. In both cases, the $C{=}O_\gamma$ bond is similar (around 1.2 Å), and both the coplanarity of the four-membered ring and the carbonylic oxygen are conserved. As already shown in the **DE**s structures, the major difference between the corresponding transition states' geometries lies in the C_9–N_1–C_2–O_α dihedral, as this is computed at 81° in $\mathbf{TS_A}$ and only −16° in $\mathbf{TS_C}$. This is further proof of the relevance of the intramolecular hydrogen bonding involving N_4–H and O_α in $\mathbf{TS_C}$.

Notably, the difference in the electronic energy computed, for both $\mathbf{TS_A}$ and $\mathbf{TS_C}$, between the ground and the first excited state is relatively small: only 17.3 kcal mol^{-1} for $\mathbf{TS_C}$ and 10.1 kcal mol^{-1} for $\mathbf{TS_A}$, indicating a possible population of the ES due to the relatively small energy gap. A relatively small gap between the ES and GS PESs is actually computed immediately after the transition state, both in the case of the A and C species (Fig. S8a and S9a).

The first singlet excited state at the transition state for both compounds basically corresponds to a (π–σ*) excitation. The examination of the Natural Transition Orbitals (NTO) associated with the hole and electron (reported in Fig. 5) shows that the hole was essentially localized in the four-membered ring with a large contribution of nitrogen (N_1) and less-relevant contributions of the central aromatic ring, the adjacent furan ring, and the oxygen atoms of the dioxetanone. The electron, on the other hand, is more strongly localized on the O_β–O_α σ* antibonding orbital. This spatial distribution highlights a modest charge-transfer component to the excitation, even though the donor and acceptor regions remain in proximity. These features confirm that the excitation involves the promotion of an electron into a ring-antibonding σ* orbital, which is consistent with a π → σ* assignment, thereby supporting the hypothesis of an asynchronous concerted process for the CO_2 elimination, starting with the O_α–O_β bond breaking.

Table 1 Main structural parameters computed for the optimized $\mathbf{DE_A}$, $\mathbf{DE_C}$, $\mathbf{TS_A}$ and $\mathbf{TS_C}$ structures. Distances in Å, angles in degrees. For labelling, refer to Schemes 1 and 2

	$\mathbf{DE_A}$	$\mathbf{DE_C}$	$\mathbf{TS_A}$	$\mathbf{TS_C}$
$d(C_2–C_3)$	1.536	1.535	1.562	1.563
$d(O_\alpha–O_\beta)$	1.465	1.464	2.102	1.943
$\Theta(O_\alpha–C_2–C_3–O_\beta)$	5.7	2.2	−2.0	−7.7
$\Theta(O_\alpha–C_2–C_3–O_\gamma)$	178.2	−176.0	171.7	173.7
$\Theta(C_9–N_1–C_2–O_\alpha)$	60.8	22.3	80.5	−15.6

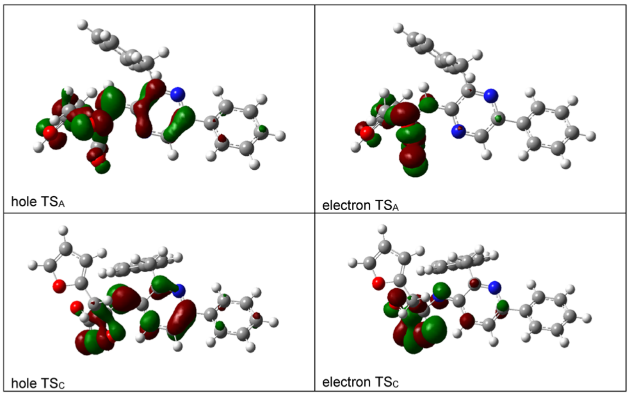

Fig. 5 NTOs corresponding to the hole and electron associated with the S_1 state computed for $\mathbf{TS_A}$ and $\mathbf{TS_C}$. All calculations are performed at the CAM-B3LYP 6-31+G(d,p) level of theory in DMSO.

The relaxation of this first excited state leads to the formation of the final product, which is an exciplex formed by the excited furimamide (**FurA*** or **FurC***) and the dissociated CO_2 molecule.

Analysing the evolution of the bond along the excited state reaction profile (Fig. 6) allows us to confirm the following claim obtained from the TD-DFT calculations: in the case of **FurA***, the reaction proceeds *via* an asynchronous concerted process characterized first by the elongation of the O_β–O_α bond occurring before the TS, followed by the cleavage of the C_2–C_3 bond. The bond breaking occurs simultaneously with the linearization of the CO_2 group, as confirmed by the trend reported in Fig. 6. A completely similar behaviour is also observed for the formation of the **FurC*** molecule (as reported in SI).

The transition-state NTOs are different from the ones characterizing the **DE** intermediates and the final product of the decomposition. Indeed, in both cases, the lowest singlet excitation is clearly a π → π* excitation, as both the hole and particle

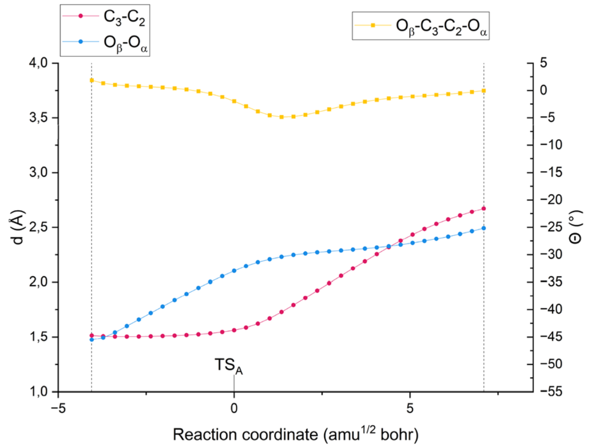

Fig. 6 Evolution of the relevant structural parameters along the ES potential energy surface, leading to the formation of the **FurA***-CO_2 exciplex.

NTOs are delocalized over the central conjugated core, with the only analogy to the TS NTOs being the relatively large N_1 contribution. This indicates a change in the transition nature, with the facilitation of the ring-opening process occurring *via* the population of a σ antibonding orbital, followed by the re-emergence of the π → π* excitation after bond breaking.

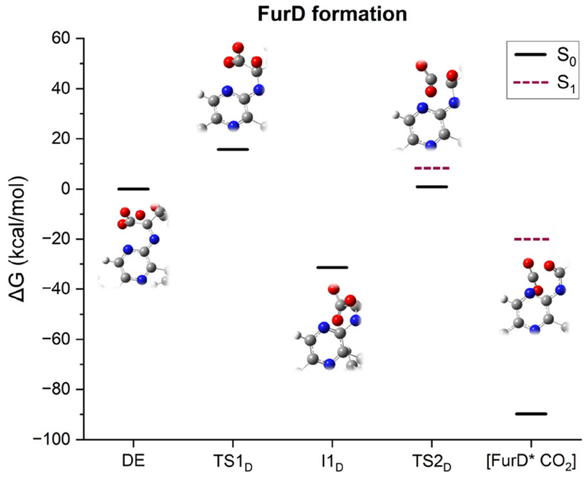

Fig. 7 Free-energy profile corresponding to the DE decomposition, leading to the formation of **FurD**. All calculations are performed at the CAM-B3LYP 6-31+G(d,p) level of theory in DMSO.

The final emissions from [**FurA*** CO_2] and [**FurC*** CO_2] are expected to occur at 361 and 416 nm, respectively, in agreement with the values for the isolated **FurA*** and **FurC*** compounds (386 nm and −411 nm).

Finally, the possibility of the decomposition of the anionic **DE** intermediate, as obtained from the C_2 and C_3 oxygenation pathways, was also considered. In this case, the reaction seems to proceed following a different mechanism altogether, as reported in Fig. 7.

The first step occurring on the GS PES is characterized by a strong charge-transfer character, as reflected by the evolution of the Mulliken charge computed on the CO_2 group, as reported in Fig. 8. During this step, the elongation of the O_α–O_β bond is accompanied by a strong distortion of the O_β–C_3–C_2–O_α dihedral and leads to the localization of a 0.75 e^- charge on the CO_2 group. This step is characterized by a large energy gap between the ground and the excited-state potential energy curves (more than 20 kcal mol^{-1}). Nonetheless, this charge transfer is followed by a quick back charge transfer, with the CO_2 group rapidly becoming neutral and detaching from the rest of the molecular structure, aligning with the second transition state geometry, as evident in Fig. 8. The decomposition takes place

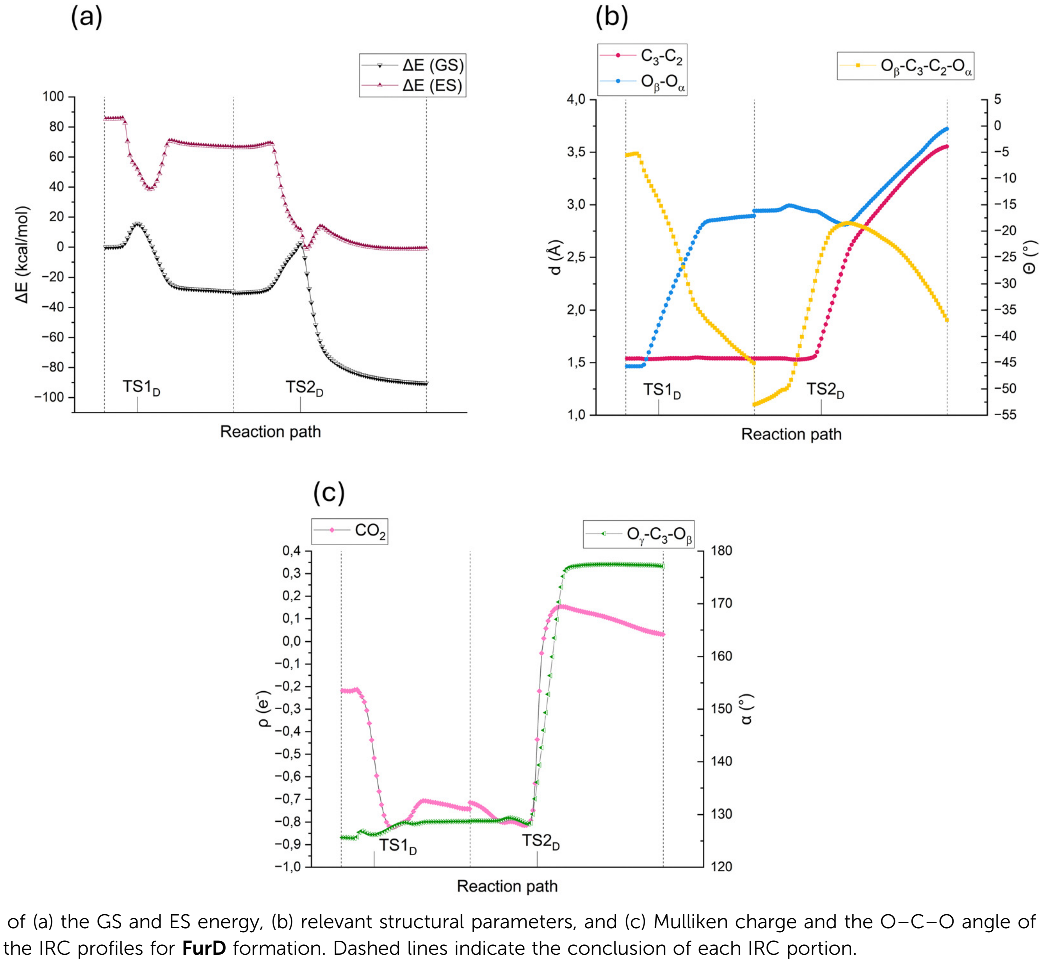

Fig. 8 Evolution of (a) the GS and ES energy, (b) relevant structural parameters, and (c) Mulliken charge and the O–C–O angle of the CO_2 fragment computed along the IRC profiles for **FurD** formation. Dashed lines indicate the conclusion of each IRC portion.

with a partial realignment of the two oxygen atoms and the reduction of the O_β–C_3–C_2–O_α dihedral, followed by an increase subsequent to the carbon dioxide elimination.

Notably, the second transition state corresponds to a strong reduction in the gap between GS and the ES, which closes up to 6.4 kcal mol^{-1} immediately after the $\mathbf{TS2_D}$ geometry, allowing for a facile population of the ES and the formation of **FurD*** after relaxation.

The NTO analysis was also performed for the intermediates and transition states for the **FurD*** formation process. In agreement with the behavior observed for $\mathbf{TS_A}$ and $\mathbf{TS_C}$, the NTOs at the first decomposition transition state of **FurD** ($\mathbf{TS1_D}$) also display a pronounced n → σ* character (as shown in Fig. S10a). By contrast, the excited state for intermediate $\mathbf{I1_D}$, which follows $\mathbf{TS1_D}$, shows a pure π → π* character. The character is very similar to the ones observed for **DE** and even for the final product, [**FurD*** CO_2], where both hole and particle NTOs are delocalized over the central conjugated core (including contributions from N_1), as highlighted in Fig. S10b. At $\mathbf{TS2_D}$, the NTOs highlight an important contribution localized on the C_2 and C_3 atoms, as reported in Fig. S10c. This delocalization underscores that $\mathbf{TS2_D}$ shows simultaneous σ*(O–O) population and C–C involvement.

A concise mechanistic picture that emerges from our NTO and energy-gap analysis is as follows. Up to $\mathbf{TS1_D}$ and through the formation of $\mathbf{I1_D}$, **FurD** decomposition occurs on the ground-state PES by concerted O_α–O_β bond cleavage and subsequent C_2–C_3 bond weakening without being able to evolve on the excited-state PES because of the large energy gap between the two. As $\mathbf{TS2_D}$ is reached, then, the gap is strongly reduced and the crossing becomes possible, leading to the definitive cleavage of the O_α–O_β bond and the subsequent breaking of the C_2–C_3 one, with CO_2 elimination as a direct consequence.

4. Conclusions

In this paper, we have provided an analysis of the reaction mechanism leading to the formation of the dioxetanone intermediate, as well as its subsequent decomposition, which is responsible for the luminescent phenomena observed. For the first step of the reaction leading to the dioxetanone process, both a C_2 and a C_3 route seem energetically possible with relatively low energy barriers, the highest of them being 7.5 kcal mol^{-1} and 15 kcal mol^{-1} for a C_2 and a C_3 attack, respectively. In both cases, the mechanism involves the formation of a peroxide, but the experimental detection of a C3 peroxide could actually be difficult due to the very low energy barriers of the steps, separating it from the dioxetanone intermediate. Anyway, our work highlights that both pathways must be considered for future studies of the reaction mechanism in a protein environment, since they are both feasible, and the protein residues could play a role in altering the energy barrier values, favouring C_2 or C_3 oxygenation.

Concerning the second step of the reaction, that is the decomposition of the dioxetanone, although we are aware of the limitations intrinsically related to the use of TD-DFT to describe diradical species and conical intersections with multireference characters, our results show how all the routes leading to the formation of **FurA**, **FurC** and **FurD** are energetically possible. Indeed, according to the obtained results, none of the three mechanisms can be *a priori* excluded, since the GS to ES-computed energy gaps are compatible with the experimental conditions. However, the mechanism leading to **FurA** presents a rate-determining step with a significantly higher barrier than the other steps. This result, together with the mismatching of its emission spectrum compared with that experimentally observed, is an indication that **FurC** and **FurD** could probably be the active species. Such a multifaceted scenario could also justify the remarkable chemiluminescence efficiency observed for this system. The inclusion and effect of the protein environment in fine-tuning the chemiluminescence mechanism are currently under analysis.

Conflicts of interest

There are no conflicts to declare.

Data availability

The data supporting this article have been included as part of the Supplementary information (SI). Supplementary information provided: additional figures showing trends of the energetic and electronic parameters (GS and ES energies, partial charges) as well as the geometric descriptors (distances, angles, and dihedrals) at the different reaction steps are provided in the SI, alongside figures of the NTOs for the **FurD** formation process. See DOI: https://doi.org/10.1039/d5cp03858h.

Acknowledgements

This work was granted access to the HPC resources of the Très Grand Centre de Calcul (TGCC) under the allocation 2024-A0150810135, made by the Grand Equipement National de Calcul Intensif (GENCI). Part of the computations were performed on the computer resources provided by CINECA as part of the agreement with the University of Milano-Bicocca (mBI25_AmbCo).

References

1 T. Jiang, L. Du and M. Li, Lighting up bioluminescence with coelenterazine: strategies and applications, *Photochem. Photobiol. Sci.*, 2016, **15**, 466–480.
2 Z. Yuan, Q. Jiang and G. Liang, Inspired by nature: Bioluminescent systems for bioimaging applications, *Talanta*, 2025, **281**, 126821.
3 C. G. England, E. B. Ehlerding and W. Cai, NanoLuc: A Small Luciferase Is Brightening Up the Field of Bioluminescence, *Bioconjugate Chem.*, 2016, **27**, 1175–1187.

4 S. Schramm and D. Weiß, Bioluminescence – The Vibrant Glow of Nature and its Chemical Mechanisms, *ChemBioChem*, 2024, **25**, e202400106.

5 P. J. Herring and E. A. Widder, in *Encyclopedia of Ocean Sciences*, ed. J. K. Cochran, H. J. Bokuniewicz and P. L. Yager, Academic Press, Oxford, 3rd edn, 2001, pp. 508–515.

6 E. A. Widder, in *Adaptive Mechanisms in the Ecology of Vision*, ed. S. N. Archer, M. B. A. Djamgoz, E. R. Loew, J. C. Partridge and S. Vallerga, Springer, Netherlands, Dordrecht, 1999, pp. 555–581.

7 S. Martini and S. H. D. Haddock, Quantification of bioluminescence from the surface to the deep sea demonstrates its predominance as an ecological trait, *Sci. Rep.*, 2017, **7**, 45750.

8 B.-W. Ding and Y.-J. Liu, Bioluminescence of Firefly Squid via Mechanism of Single Electron-Transfer Oxygenation and Charge-Transfer-Induced Luminescence, *J. Am. Chem. Soc.*, 2017, **139**, 1106–1119.

9 Z. M. Kaskova, A. S. Tsarkova and I. V. Yampolsky, 1001 lights: luciferins, luciferases, their mechanisms of action and applications in chemical analysis, biology and medicine, *Chem. Soc. Rev.*, 2016, **45**, 6048–6077.

10 A. Schenkmayerova, M. Toul, D. Pluskal, R. Baatallah, G. Gagnot, G. P. Pinto, V. T. Santana, M. Stuchla, P. Neugebauer, P. Chaiyen, J. Damborsky, D. Bednar, Y. L. Janin, Z. Prokop and M. Marek, Catalytic mechanism for Renilla-type luciferases, *Nat. Catal.*, 2023, **6**, 23–38.

11 E. Brodl, A. Winkler and P. Macheroux, Molecular Mechanisms of Bacterial Bioluminescence, *Comput. Struct. Biotechnol. J.*, 2018, **16**, 551–564.

12 B. R. Branchini, T. L. Southworth, D. M. Fontaine, D. Kohrt, M. Talukder, E. Michelini, L. Cevenini, A. Roda and M. J. Grossel, An enhanced chimeric firefly luciferase-inspired enzyme for ATP detection and bioluminescence reporter and imaging applications, *Anal. Biochem.*, 2015, **484**, 148–153.

13 M. H. Degeling, M. S. S. Bovenberg, G. K. Lewandrowski, M. C. de Gooijer, C. L. A. Vleggeert-Lankamp, M. Tannous, C. A. Maguire and B. A. Tannous, Directed Molecular Evolution Reveals Gaussia Luciferase Variants with Enhanced Light Output Stability, *Anal. Chem.*, 2013, **85**, 3006–3012.

14 S. Inouye, J. Sato, Y. Sahara-Miura, S. Yoshida and T. Hosoya, Luminescence enhancement of the catalytic 19 kDa protein (KAZ) of Oplophorus luciferase by three amino acid substitutions, *Biochem. Biophys. Res. Commun.*, 2014, **445**, 157–162.

15 H.-W. Yeh, O. Karmach, A. Ji, D. Carter, M. M. Martins-Green and H. Ai, Red-shifted luciferase–luciferin pairs for enhanced bioluminescence imaging, *Nat. Methods*, 2017, **14**, 971–978.

16 S. Iwano, M. Sugiyama, H. Hama, A. Watakabe, N. Hasegawa, T. Kuchimaru, K. Z. Tanaka, M. Takahashi, Y. Ishida, J. Hata, S. Shimozono, K. Namiki, T. Fukano, M. Kiyama, H. Okano, S. Kizaka-Kondoh, T. J. McHugh, T. Yamamori, H. Hioki, S. Maki and A. Miyawaki, Single-cell bioluminescence imaging of deep tissue in freely moving animals, *Science*, 2018, **359**, 935–939.

17 T. Nagai and M. Hattori, Tiny but bright, *Nat. Rev. Chem.*, 2022, **6**, 522–523.

18 M. P. Hall, J. Unch, B. F. Binkowski, M. P. Valley, B. L. Butler, M. G. Wood, P. Otto, K. Zimmerman, G. Vidugiris, T. Machleidt, M. B. Robers, H. A. Benink, C. T. Eggers, M. R. Slater, P. L. Meisenheimer, D. H. Klaubert, F. Fan, L. P. Encell and K. V. Wood, Engineered Luciferase Reporter from a Deep Sea Shrimp Utilizing a Novel Imidazopyrazinone Substrate, *ACS Chem. Biol.*, 2012, **7**, 1848–1857.

19 A. S. Dixon, M. K. Schwinn, M. P. Hall, K. Zimmerman, P. Otto, T. H. Lubben, B. L. Butler, B. F. Binkowski, T. Machleidt, T. A. Kirkland, M. G. Wood, C. T. Eggers, L. P. Encell and K. V. Wood, NanoLuc Complementation Reporter Optimized for Accurate Measurement of Protein Interactions in Cells, *ACS Chem. Biol.*, 2016, **11**, 400–408.

20 F. X. Schaub, Md. S. Reza, C. A. Flaveny, W. Li, A. M. Musicant, S. Hoxha, M. Guo, J. L. Cleveland and A. L. Amelio, Fluorophore-NanoLuc BRET Reporters Enable Sensitive In Vivo Optical Imaging and Flow Cytometry for Monitoring Tumorigenesis, *Cancer Res.*, 2015, **75**, 5023–5033.

21 L. Biewenga, B. J. H. M. Rosier and M. Merkx, Engineering with NanoLuc: a playground for the development of bioluminescent protein switches and sensors, *Biochem. Soc. Trans.*, 2020, **48**, 2643–2655.

22 A. Bonardi, M. Turelli, G. Moro, U. Cosentino, C. Greco and C. Adamo, Behind the glow: unveiling the nature of NanoLuc reactants and products, *Phys. Chem. Chem. Phys.*, 2024, **26**, 27447–27458.

23 M. Nemergut, D. Pluskal, J. Horackova, T. Sustrova, J. Tulis, T. Barta, R. Baatallah, G. Gagnot, V. Novakova, M. Majerova, S. M. Marques, M. Toul, J. Damborsky, D. Bednar, Z. Prokop and Y. L. Janin, Illuminating the mechanism and allosteric behavior of NanoLuc luciferase, *Nat. Commun.*, 2023, **14**, 7864.

24 C. M. Magalhães, J. C. G. Esteves da Silva and L. Pinto da Silva, Comparative study of the chemiluminescence of coelenterazine, coelenterazine-e and *Cypridina* luciferin with an experimental and theoretical approach, *J. Photochem. Photobiol., B*, 2019, **190**, 21–31.

25 J.-M. Xie, Y. Leng, X.-Y. Cui, C.-G. Min, A.-M. Ren, G. Liu and Q. Yin, Theoretical Study on the Formation and Decomposition Mechanisms of Coelenterazine Dioxetanone, *J. Phys. Chem. A*, 2023, **127**, 3804–3813.

26 B. R. Branchini, C. E. Behney, T. L. Southworth, D. M. Fontaine, A. M. Gulick, D. J. Vinyard and G. W. Brudvig, Experimental Support for a Single Electron-Transfer Oxidation Mechanism in Firefly Bioluminescence, *J. Am. Chem. Soc.*, 2015, **137**, 7592–7595.

27 H. Isobe, S. Yamanaka, S. Kuramitsu and K. Yamaguchi, Regulation Mechanism of Spin−Orbit Coupling in Charge-Transfer-Induced Luminescence of Imidazopyrazinone Derivatives, *J. Am. Chem. Soc.*, 2008, **130**, 132–149.

28 C.-G. Min, Q.-B. Liu, Y. Leng, C. M. Magalhães, S.-J. Huang, C.-X. Liu, X.-K. Yang and L. P. da Silva, Mechanistic Insight into the Chemiluminescent Decomposition of Cypridina Dioxetanone and the Chemiluminescent, Fluorescent

Properties of the Light Emitter of Cypridina Bioluminescence, *J. Chem. Inf. Model.*, 2019, **59**, 4393–4401.

29 L. Pinto da Silva, A. J. M. Santos and J. C. G. Esteves da Silva, Efficient Firefly Chemi/Bioluminescence: Evidence for Chemiexcitation Resulting from the Decomposition of a Neutral Firefly Dioxetanone Molecule, *J. Phys. Chem. A*, 2013, **117**, 94–100.

30 C. Gao, Y. Wu, C. Fitzgerald, H. Wang, T. Ugo, T. Uyeda, W. Zhou, Y. Su, T. A. Kirkland and M. Z. Lin, An optimized luciferin formulation for NanoLuc-based in vivo bioluminescence imaging, *Sci. Rep.*, 2025, **15**, 12884.

31 L. Pinto da Silva, R. F. J. Pereira, C. M. Magalhães and J. C. G. Esteves da Silva, Mechanistic Insight into Cypridina Bioluminescence with a Combined Experimental and Theoretical Chemiluminescent Approach, *J. Phys. Chem. B*, 2017, **121**, 7862–7871.

32 M. Sahihi, J. S. Garcìa and I. Navizet, Bioluminescent Nanoluciferase−Furimamide Complex: A Theoretical Study on Different Protonation States, *J. Phys. Chem. B*, 2020, **124**, 2539–2548.

33 S.-F. Chen, N. Ferré and Y.-J. Liu, QM/MM Study on the Light Emitters of Aequorin Chemiluminescence,Bioluminescence, and Fluorescence: A General Understanding of theBioluminescence of Several Marine Organisms, *Chem. – Eur. J.*, 2013, **19**, 8466–8472.

34 F. McCapra and Y. C. Chang, The Chemiluminescence of a Cypridina Luciferin Analogue, *Chem. Commun.*, 1967, 1011–1012.

35 M. J. Frisch, G. W. Trucks, H. B. Schlegel, G. E. Scuseria, M. A. Robb, J. R. Cheeseman, G. Scalmani, V. Barone, G. A. Petersson, H. Nakatsuji, X. Li, M. Caricato, A. V. Marenich, J. Bloino, B. G. Janesko, R. Gomperts, B. Mennucci, H. P. Hratchian, J. V. Ortiz, A. F. Izmaylov, J. L. Sonnenberg, D. Williams-Young, F. Ding, F. Lipparini, F. Egidi, J. Goings, B. Peng, A. Petrone, T. Henderson, D. Ranasinghe, V. G. Zakrzewski, J. Gao, N. Rega, G. Zheng, W. Liang, M. Hada, M. Ehara, K. Toyota, R. Fukuda, J. Hasegawa, M. Ishida, T. Nakajima, Y. Honda, O. Kitao, H. Nakai, T. Vreven, K. Throssell, J. A. Montgomery, Jr., J. E. Peralta, F. Ogliaro, M. J. Bearpark, J. J. Heyd, E. N. Brothers, K. N. Kudin, V. N. Staroverov, T. A. Keith, R. Kobayashi, J. Normand, K. Raghavachari, A. P. Rendell, J. C. Burant, S. S. Iyengar, J. Tomasi, M. Cossi, J. M. Millam, M. Klene, C. Adamo, R. Cammi, J. W. Ochterski, R. L. Martin, K. Morokuma, O. Farkas, J. B. Foresman and D. J. Fox, *Gaussian 16, Revision C.01*, Gaussian, Inc., Wallingford CT, 2016.

36 T. Yanai, D. P. Tew and N. C. Handy, A new hybrid exchange–correlation functional using the Coulomb-attenuating method (CAM-B3LYP), *Chem. Phys. Lett.*, 2004, **393**, 51–57.

37 R. Ditchfield, W. J. Hehre and J. A. Pople, Self-Consistent Molecular-Orbital Methods. IX. An Extended Gaussian-Type Basis for Molecular-Orbital Studies of Organic Molecules, *J. Chem. Phys.*, 2003, **54**, 724–728.

38 W. J. Hehre, R. Ditchfield and J. A. Pople, Self—Consistent Molecular Orbital Methods. XII. Further Extensions of Gaussian—Type Basis Sets for Use in Molecular Orbital Studies of Organic Molecules, *J. Chem. Phys.*, 2003, **56**, 2257–2261.

39 M. M. Francl, W. J. Pietro, W. J. Hehre, J. S. Binkley, M. S. Gordon, D. J. DeFrees and J. A. Pople, Self-consistent molecular orbital methods. XXIII. A polarization-type basis set for second-row elements, *J. Chem. Phys.*, 1982, **77**, 3654–3665.

40 P. C. Hariharan and J. A. Pople, The influence of polarization functions on molecular orbital hydrogenation energies, *Theor. Chim. Acta*, 1973, **28**, 213–222.

41 H. Isobe, S. Yamanaka, M. Okumura and K. Yamaguchi, Theoretical Investigation of Thermal Decomposition of Peroxidized Coelenterazines with and without External Perturbations, *J. Phys. Chem. A*, 2009, **113**, 15171–15187.

42 L. Yue, Y.-J. Liu and W.-H. Fang, Mechanistic Insight into the Chemiluminescent Decomposition of Firefly Dioxetanone, *J. Am. Chem. Soc.*, 2012, **134**, 11632–11639.

43 G. Santra, R. Calinsky and J. M. L. Martin, Benefits of Range-Separated Hybrid and Double-Hybrid Functionals for a Large and Diverse Data Set of Reaction Energies and Barrier Heights, *J. Phys. Chem. A*, 2022, **126**, 5492–5505.

44 J. Tomasi, B. Mennucci and R. Cammi, Quantum Mechanical Continuum Solvation Models, *Chem. Rev.*, 2005, **105**, 2999–3094.

45 V. Barone and M. Cossi, Quantum Calculation of Molecular Energies and Energy Gradients in Solution by a Conductor Solvent Model, *J. Phys. Chem. A*, 1998, **102**, 1995–2001.

46 M. Cossi, N. Rega, G. Scalmani and V. Barone, Energies, structures, and electronic properties of molecules in solution with the C-PCM solvation model, *J. Comput. Chem.*, 2003, **24**, 669–681.

47 K. Usami and M. Isobe, Low-temperature photooxygenation of coelenterate luciferin analog synthesis and proof of 1,2-dioxetanone as luminescence intermediate, *Tetrahedron*, 1996, **52**, 12061–12090.

48 I. Navizet, Y.-J. Liu, N. Ferré, D. Roca-Sanjuán and R. Lindh, The Chemistry of Bioluminescence: An Analysis of Chemical Functionalities, *ChemPhysChem*, 2011, **12**, 3064–3076.

49 F. Liu, Y. Liu, L. De Vico and R. Lindh, Theoretical Study of the Chemiluminescent Decomposition of Dioxetanone, *J. Am. Chem. Soc.*, 2009, **131**, 6181–6188.

50 B.-W. Ding, P. Naumov and Y.-J. Liu, Mechanistic Insight into Marine Bioluminescence: Photochemistry of the Chemiexcited *Cypridina* (Sea Firefly) Lumophore, *J. Chem. Theory Comput.*, 2015, **11**, 591–599.